Engineering RNA–Protein Complexes with Different Shapes for Imaging and Therapeutic Applications

Eriko Osada,[†] Yuki Suzuki,[‡,§] Kumi Hidaka,[∥] Hirohisa Ohno,[⊥] Hiroshi Sugiyama,[‡,§,∥] Masayuki Endo,[§,∥] and Hirohide Saito[†,¶,*]

[†]Center for iPS Cell Research and Application, Kyoto University, 53 Kawahara-cho, Shogoin, Sakyo-ku, Kyoto 606-8507, Japan, [‡]Department of Chemistry, Graduate School of Science, Kyoto University, Kitashirakawa Oiwake-cho, Sakyo-ku, Kyoto 606-8502, Japan, [§]CREST, Japan Science and Technology Corporation (JST), Sanbancho, Chiyoda-ku, Tokyo 102-0075, Japan, [⊥]Laboratory of Gene Biodynamics, Graduate School of Biostudies, Kyoto University, Kitashirakawa Oiwake-cho, Sakyo-ku, Kyoto 606-8502, Japan, [∥]Institute for Integrated Cell-Material Sciences (WPI-iCeMS), Kyoto University, Yoshida-Ushinomiya-cho, Sakyo-ku, Kyoto 606-8501, Japan, and [¶]The Hakubi Center for Advanced Research, Kyoto University, Yoshida-Ushinomiya-cho, Sakyo-ku, Kyoto 606-8501, Japan

ABSTRACT Molecular machines composed of RNA–protein (RNP) complexes may expand the fields of molecular robotics, nanomedicine, and synthetic biology. However, constructing and directly visualizing a functional RNP nanostructure to detect and control living cell function remains a challenge. Here we show that RNP nanostructures with modular functions can be designed and visualized at single-RNP resolution in real time. The RNP structural images collected in solution through high-speed atomic force microscopy showed that a single RNP interaction induces a conformational change in the RNA scaffold, which supports the nanostructure formation designed. The specific RNP interaction also improved RNA nanostructure stability in a serum-containing buffer. We developed and visualized functional RNPs (*e.g.*, to detect human cancer cells or knockdown target genes) by attaching a protein or RNA module to the same RNA scaffold of an optimal size. The synthetic RNP architecture may provide alternative materials to detect and control functions in target mammalian cells.

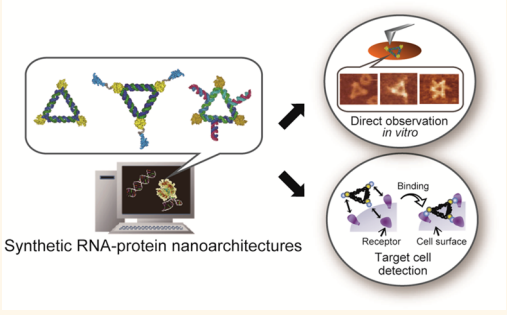

KEYWORDS: RNA · RNA–protein interaction · RNP nanostructures · RNA nanotechnology · high-speed atomic force microscopy · RNAi · nanomedicine

In naturally occurring systems, RNA–protein (RNP) complexes (*e.g.*, the ribosome and spliceosome) play important roles to modulate a variety of cellular functions.[1−3] For example, the ribosome is a sophisticated RNP-based molecular machine that catalyzes protein synthesis in all living organisms.[4] Specific RNP interactions and protein-induced RNA conformational changes are important for the construction of functional RNP molecules in many cases.[5−7] However, the development of functional RNP nanostructures and direct observation of native RNP interaction (*e.g.*, without chemical or fluorescent labeling) at high resolution remains a challenge. Thus, we aimed to construct and visualize functional RNP nanostructures in which the RNA-binding protein specifically regulates the RNA conformation.

Recently, DNA-based molecular nanomachines[8,9] have been designed and constructed to control biochemical reactions *in vitro*[10,11] and manipulate living cells.[12−15] In addition to DNA-based machines,[16] RNA nanostructures[17−21] may provide alternative materials with which to control target cell functions. In principle, a synthetic RNA can have multiple functions outside (*e.g.*, cell detection) and inside cells (*e.g.*, gene expression control) by inserting functional modules into the RNA scaffold.[22−27] Several synthetic RNA nanostructures have been constructed to control gene expression and function of mammalian cells.[28−30] However, development of protein-controlled RNA nanostructures, in which functional protein modules can be precisely placed in nanometer-scale on the RNA scaffold to control functions in target mammalian cells remains elusive. To expand the functionality and modularity of RNP nanostructures, it is important to directly and precisely observe the designed nanostructures in solution.

* Address correspondence to hirohide.saito@cira.kyoto-u.ac.jp.

Received for review April 24, 2014 and accepted July 24, 2014.

Published online July 24, 2014
10.1021/nn502253c

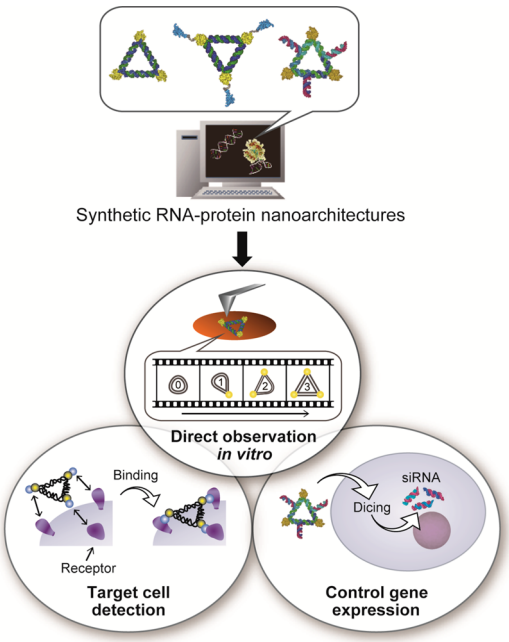

Figure 1. Schematic description of synthetic RNP nanostructure construction, direct imaging, and mammalian cell applications. Synthetic RNP nanostructures can be designed *in silico* (top). The shape and conformational change of the RNP nanostructures in solution can be directly visualized using HS-AFM in time-lapse at a high resolution (bottom middle). Functional RNPs that selectively recognize target cells (bottom left) or control gene expression in cells (bottom right) can also be constructed and visualized.

We can evaluate the RNP architecture design *in vitro* and then optimize their functions for cellular applications by using the appropriate RNPs.

In this study, we designed and directly visualized the formation of RNP nanostructures in solution at a single-RNP-interaction resolution (Figure 1, top and bottom center). Direct imaging of the RNP interaction showed that the RNA scaffold shape was regulated dynamically by the RNA-binding protein. In addition, we designed and observed the functional RNP nanoarchitecture for mammalian cell applications (Figure 1, bottom left and right). We developed two functional RNP nanostructures: one facilitated binding and detection for a specific breast cancer cell line, and the other modulated gene expression in cells. The RNP can be designed in a modular manner by incorporating a functional protein or RNA module into the same RNA scaffold of an optimal size and improved stability *via* the tight RNP interaction. This is a promising method for generating functional RNP nanostructures for future therapeutic applications.

RESULTS

Direct Observation of Synthetic RNP Nanostructures in Solution. We previously designed and constructed synthetic RNP nanostructures with an equilateral triangle shape (*Tri*-RNP) using the ribosomal protein L7Ae and the kink-turn (K-turn) RNA motif responsible for binding.[31] L7Ae tightly interacts with the K-turn and induces a conformational change in the K-turn RNA, which bends by approximately 60°.[5,32−34] Taking advantage of the strong and specific interaction, in the present study, we used our *Tri*-RNP system as a basic molecular scaffold upon which to assemble protein or RNA modules and generate functional RNP nanostructures. We first designed and constructed the synthetic *Tri*-RNPs with five different sizes, ranging from side lengths of approximately 14 to 34 nm (Supporting Information Figures S1−S5). We incorporated three K-turn RNA motifs into the three vertices of our triangular nanostructures. One side of each triangle was designed with 15, 26, 48, 70, and 92 base pairs of dsRNAs comprising L-RNA and S-RNA. The LS-RNAs formed are referred to as LS-15, LS-26, LS-48, LS-70, and LS-92. We expected that the L7Ae-K-turn interactions at the three vertices would facilitate the formation of triangular structures with five different sizes, referred to as *Tri*-15, *Tri*-26, *Tri*-48, *Tri*-70, and *Tri*-92, which correspond to the side lengths of 13.7, 16.7, 22.6, 28.5, and 34.4 nm, respectively. Accordingly, we prepared the LS-RNAs and analyzed the L7Ae-LS-RNA interactions using an electrophoretic mobility shift assay (EMSA) (Supporting Information Figure S6a−e). As expected, we observed the corresponding L7Ae-LS-RNA interactions in all of the designed constructs.

Next, we directly visualized the RNP nanostructures in solution. We previously analyzed the triangular RNPs (*Tri*-26 and *Tri*-48) through conventional atomic force microscopy (AFM).[31] However, it remains a challenge to visualize the RNP nanostructures at single-RNP-interaction resolution. Our previous studies also analyzed the RNP nanostructures under air conditions, under which it is difficult to observe the RNA conformational changes both at high resolution and by time-lapse imaging. Recently, state-of-the-art high-speed AFM (HS-AFM)[35] has been successfully used to capture DNA and protein structures at high resolution.[36−38] Thus, we used HS-AFM to analyze the RNP nanostructures and L7Ae-induced RNA conformational changes in solution.

We first analyzed the LS-RNAs without L7Ae (Figure 2a, bottom, −L7Ae). The LS-RNAs of the five different sizes exhibited closed circular structures composed of a dsRNA. The RNA-only structure shapes in solution were heterogeneous, which indicates that the LS-RNA structures were flexible without L7Ae, which is consistent with previous reports.[31] In contrast, with L7Ae, we clearly observed equilateral triangular nanostructures at a single-RNP-interaction resolution. We detected three individually bound L7Ae proteins as "dots" at the three vertices of the *Tri*-RNPs and a triangular RNA scaffold "cavity" generated by the three dsRNA sides (Figure 2a, top, +L7Ae). In addition, the RNP triangular shapes were homogeneous compared with the RNA-only structures, which confirms that the L7Ae-K-turn interaction dynamically induces the RNA

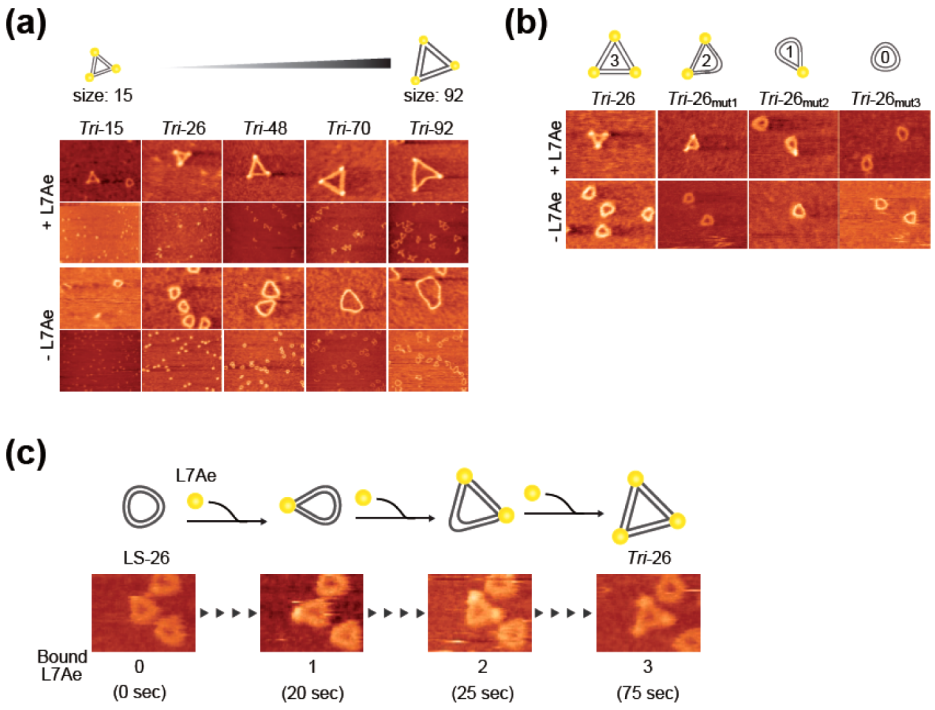

Figure 2. Direct observation of RNP nanostructures in solution using HS-AFM. (a) Direct visualization of the RNA and RNP nanostructures with five different sizes (*Tri*-15, *Tri*-26, *Tri*-48, *Tri*-70, and *Tri*-92). The dsRNA regions are composed of two RNA strands: L- and S-strand RNA (LS-RNA). The top two rows of panels are the AFM images of 50 nM LS-RNA with 300 nM L7Ae. The bottom two rows of panels are 50 nM LS-RNA without L7Ae. The AFM images were acquired on two different scales (first and third panels, 100 nm × 75 nm; second and fourth panels, 500 nm × 375 nm). (b) Effect of the number of K-turns on triangular formation. One, two, or three defective K-turns were incorporated into the each *Tri*-26 vertex, which generated three *Tri*-26 mutant variants. AFM images of 50 nM LS-RNA with 300 nM L7Ae (top) or without L7Ae (bottom) are shown. AFM images (100 nm × 75 nm). (c) Snapshots of the RNP nanostructure during successive HS-AFM analysis. A schematic illustration of the L7Ae-induced RNA conformational change is also shown. The corresponding image was extracted from the time-lapse images (60 nm × 45 nm, see also Supporting Information Figure S8a and movies S1 and S2).

conformational change in solution. The *Tri*-92 triangular shapes was relatively variable (*e.g.*, the bent dsRNA region) compared with the other samples, although L7Ae interacted similarly with the three K-turn motifs in each LS-RNA construct (Figure 2a, top, and Supporting Information Figure S6a–e). This observation may indicate that the triangular formation of *Tri*-92 may be unstable due to the longer length of its dsRNA.

To further confirm that the three L7Ae-K-turn interactions are important for the formation of the triangular nanostructures, we incorporated the mutated K-turn motif into one, two, or three *Tri*-26 vertices (referred to as *Tri*-26$_{mut1}$, *Tri*-26$_{mut2}$, and *Tri*-26$_{mut3}$, respectively) (Figure 2b). An analysis of the RNP interaction using EMSA confirmed that our variants interacted with the corresponding number of L7Ae (two, one, and zero, respectively) (Supporting Information Figure S6f). As expected, we directly observed the corresponding number of RNP interactions on the RNA scaffold using AFM. We observed either two, one, or zero L7Ae dots on *Tri*-26$_{mut1}$, *Tri*-26$_{mut2}$, and *Tri*-26$_{mut3}$, respectively, with L7Ae (Figure 2b, top), whereas circular-shaped LS-RNA structures were observed for all constructs in the absence of L7Ae (Figure 2b, bottom). Statistical analyses of the structures confirmed the expected number of L7Ae-K-turn interactions on the designed RNA scaffold (Supporting Information Figure S7). These results confirm that three L7Ae-K-turn interactions at the three vertices are indispensable for inducing triangular RNP formation.

Detecting the RNP Interaction and RNA Conformational Change by Time-Lapse Imaging. Next, we analyzed the protein-induced RNA conformational change and triangular nanostructure formation through successive HS-AFM images. The RNA nanostructures composed of LS-26 were adsorbed onto a mica surface; an excessive level of L7Ae was then added to monitor conformational change in the RNA nanostructure. Interestingly, we successfully monitored the RNP interaction and the L7Ae-induced RNA conformational change through HS-AFM (Figure 2c and Supporting Information Figure S8a and movies S1 and S2). The time-lapse images show that L7Ae directly induced a conformational change in each of the three LS-26-K-turn RNA regions, which were bent by approximately 60°, and dynamically transformed the shape of the nanostructures from a flexible circular form (LS-26) to a rigid triangular structure (*Tri*-26) in a stepwise manner. In contrast, we also observed a structural transition from the stable RNP to the flexible circular RNA, which was facilitated by protein dissociation from RNA (Supporting Information Figure S8b). To our knowledge, this is the first

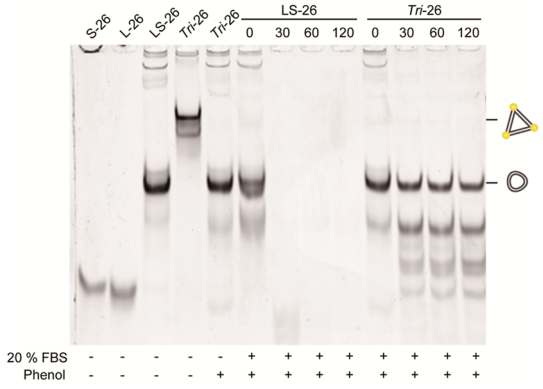

Figure 3. Analysis of LS-RNA/*Tri*-RNP stabilities in the presence of serum. The LS-26/*Tri*-26 stabilities were analyzed with FBS. LS-26 or *Tri*-26 was incubated with 20% FBS at 37 °C for 0, 30, 60, and 120 min.

example of a single RNP interaction and, thus, a protein-induced RNA conformational change directly visualized in solution and in a native state without any chemical or fluorescent labeling.

Improved RNA Nanostructure Stability *via* Specific RNP Interactions. Next, we analyzed the stability of the RNP nanostructures in the presence of serum. Previous studies reported that the RNA nanostructure stability was enhanced with modified nucleotides.[19,29] We investigated whether the tight and specific RNP interaction would also improve RNA stability. The RNP interactions on the LS-26 scaffold enhanced the RNA nanostructure stability in fetal bovine serum (FBS)-containing buffer (Figure 3). Without L7Ae, LS-26 was immediately degraded in 30 min in 20% FBS, whereas the three L7Ae-K-turn interactions on the RNA scaffold (*Tri*-26) improved RNA stability despite the absence of chemically modified RNA nucleotides. *Tri*-26_{mut3} did not improve RNA stability with L7Ae (Supporting Information Figure S9a), which indicates that the specific L7Ae-K-turn interaction increased RNA stability. Similar results were observed with human serum (Supporting Information Figure S9b). These results indicate that the RNP interaction improved RNA nanostructure stability under physiological conditions (*e.g.*, in the presence of bovine or human serum).

Construction of Functional RNP Nanostructures That Can Bind and Detect a Target Breast Cancer Cell Line. In principle, we can place desired protein modules fused to L7Ae on the RNA scaffold in nanometer-scale and optimize their function and configuration. Thus, we first investigated whether the triangular RNP nanostructures could be used as scaffolds to maintain function of protein modules that can bind and detect specific cancer cells (Figure 4a,b). To design and construct such functional RNPs that selectively recognize target breast cancer cells and deliver the RNA scaffold to the cell surface, we prepared an affibody$_{ZHER2:342}$ peptide fused to L7Ae (referred to here as L7Ae-AFB). The affibody$_{ZHER2:342}$ interacts with the cell surface HER2 receptor on several breast cancer cells with high affinity (K_D = 22 pM) and specificity.[39,40] Accordingly, we designed triangular RNPs with an LS-RNA region and L7Ae-AFB at three vertices (referred to as *Tri*-AFB, Figure 4a). The *Tri*-AFB should selectively bind and detect the target breast cancer cell *via* the three AFB peptides on the RNA triangular scaffold (Figure 4b). We investigated the interaction between L7Ae-AFB and LS-26 and the *Tri*-26-AFB structure *in vitro*. Using EMSAs, we confirmed that L7Ae-AFB bound the K-turn motif similar to the parental L7Ae-K-turn (Supporting Information Figure S10). We next analyzed the *Tri*-AFB structure in solution through AFM. We confirmed that the triangular structures were maintained with L7Ae-AFB. We directly observed three AFB peptides attached to the three *Tri*-26 vertices (Figure 4c, white arrows), which confirmed that the RNP nanostructure with functional peptide modules was constructed as designed.

We next tested the *Tri*-AFB capacity for binding at the target breast cancer cell surfaces. To screen for an effective binder, we designed *Tri*-AFBs with five different sizes and tested the interaction between the *Tri*-AFBs and target breast cancer cell line SKBR3 (HER2-high positive cell). We added the *Tri*-AFBs with Alexa-647-labeled LS-RNA to the cell culture medium (Opti-MEM), which was incubated for 1 h, and tested its cell-binding ability (Alexa-647-labeled RNA was used to directly monitor the cell-binding ability of the RNA nanostructures, Figure 4b). Flow cytometry analysis showed that, although each *Tri*-AFB interacted with the SKBR3 cell surface, *Tri*-26-AFB recognized the SKBR3 cells most effectively, whereas *Tri*-70-AFB and *Tri*-92-AFB exhibited comparatively lower binding (Figure 4d). Thereafter, we focused on *Tri*-26-AFB.

To investigate the capacity for selective cell recognition of *Tri*-26-AFB, we next tested the interaction between *Tri*-26-AFB and three different breast cancer cell lines: the target SKBR3 and nontargets MCF-7 (HER2-low) and MDA-MB-231 (HER2-negative). Flow cytometry and confocal microscopy analyses showed that *Tri*-26-AFB selectively interacted with SKBR3 cells, whereas it did not recognize MCF-7 and MDA-MB-231 cells (Figure 4e,f and Supporting Information Figure S11a–c). These findings suggest that the interaction between *Tri*-26-AFB and HER2 on the cell surface is responsible for selective SKBR3 cell recognition. Furthermore, we employed *Tri*-26 mutant variants (*Tri*-26_{mut1}, *Tri*-26_{mut2}, and *Tri*-26_{mut3}) to investigate the relationship between the number of AFB on the RNA scaffold and the SKBR3 cells' binding ability. The number of AFB on the RNA scaffold was positively correlated with the cell-binding affinity (Figure 4g and Supporting Information Figure S11d), which indicates that increasing the number of AFB–HER2 interactions on the same RNA scaffold may enhance recognition of the target HER2. Together, these findings indicate that the RNP nanostructures at an optimal size (*e.g.*, *Tri*-26-AFB) selectively and effectively recognize the target

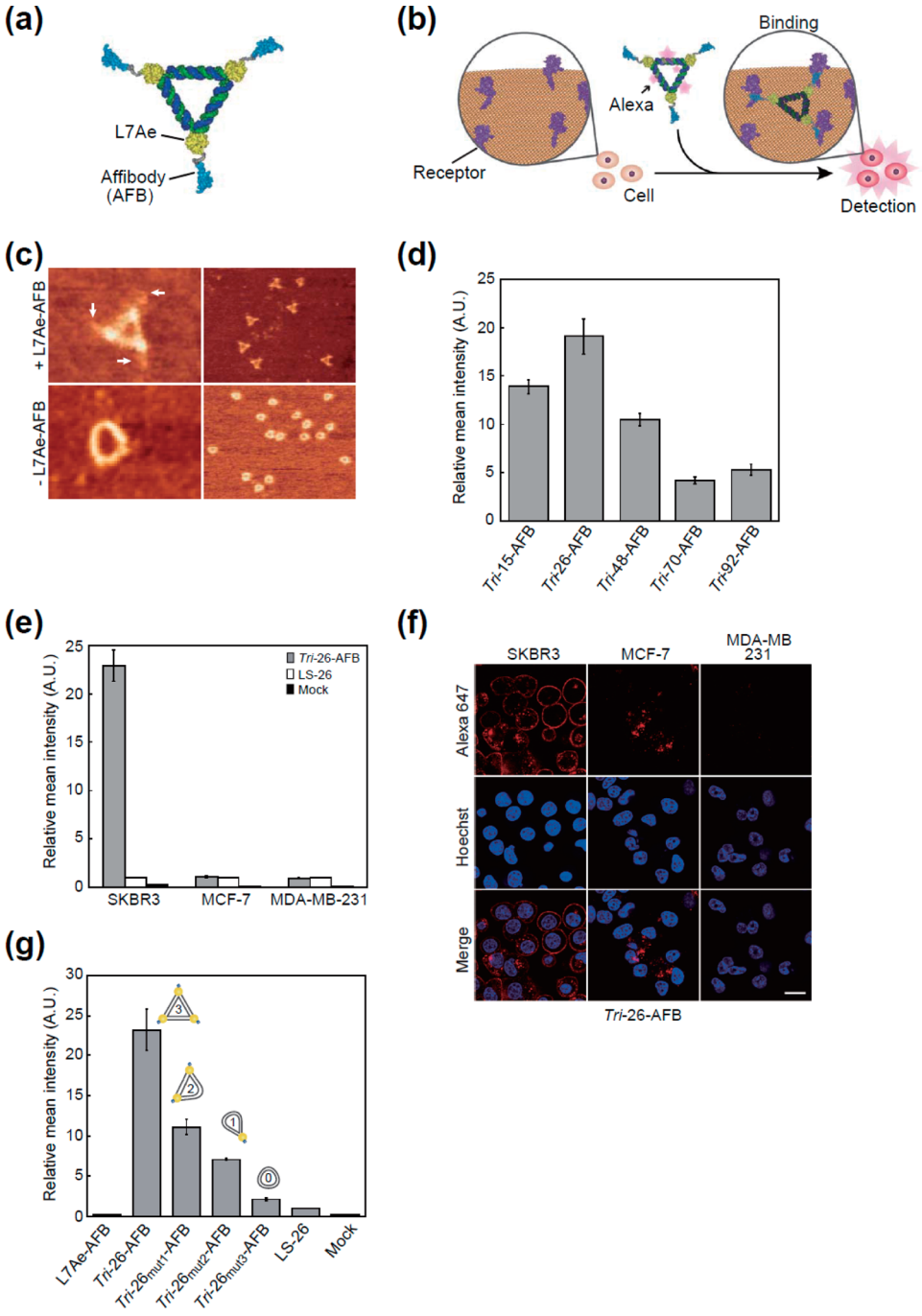

Figure 4. Selective recognition and detection of target cells using *Tri*-AFB nanostructures. (a) Position of the three AFBs fused to three L7Ae on each vertex of *Tri*-26 is shown. AFB peptides and a flexible linker are shown as blue and gray, respectively. (b) Schematic representation of *Tri*-AFB specific recognition and detection of the target cell. The *Tri*-AFB with Alexa-647-labeled RNA selectively binds the cell surface HER2 receptors and detects target cells. (c) AFM images of LS-26 with (top) or without L7Ae-AFB (bottom). AFM images (60 nm × 45 nm, left, and 300 nm × 225 nm, right). (d) Screening an effective *Tri*-AFB to recognize SKBR3 cell. *Tri*-AFBs with five different sizes were analyzed for SKBR3 recognition using flow cytometer (see Supplementary Methods). The data are presented as the mean ± SD of triplicate experiments (n = 3). (e) *Tri*-26-AFB target cell selectivity. Three breast cancer cell lines were used for the analysis. The cells were treated with 10 nM *Tri*-26-AFB or LS-26. Target cell selectivity was analyzed using flow cytometry. The data are the mean ± SD of triplicate experiments (n = 3). (f) Fluorescent microscopy analysis of *Tri*-26-AFB with the three cell lines. The cells were treated using the same procedure in (e) and analyzed using confocal microscopy (see also Supporting Information Figure S11a,b). The scale bar indicates 20 μm. (g) *Tri*-26 mutant assays to investigate the relationship between the number of AFB on the RNA scaffold and the cell-binding capacity. The cells were treated with 10 nM *Tri*-26-AFB variants or 30 nM L7Ae-AFB. The cell-binding abilities of these variants were analyzed using a flow cytometer. The data are the mean ± SD of triplicate experiments (n = 3). Mock indicates the buffer-treated cells.

breast cancer cell receptor and can deliver the RNA scaffold to the target cell surface.

We also investigated whether different shapes of RNP nanostructures can be employed as an alternative

scaffold to detect target cells. Thus, we designed and constructed a tetragon RNP nanostructure (*Tetra*-RNP) that contains four L7Ae-K-turn interaction motifs (Supporting Information Figures S12 and S13a). EMSA assay confirmed the corresponding L7Ae-K-turn interaction of *Tetra*-RNP (Supporting Information Figure S13b), and flow cytometry analysis showed that *Tetra*-AFB can bind to target SKBR3 cells in a manner similar to *Tri*-AFB (Supporting Information Figure S13c). These results indicate that *Tetra*-RNP in addition to *Tri*-RNP recognizes the target cells selectively. While *Tetra*-RNP nanostructure can bind up to four L7Ae proteins (contains four K-turn motifs), only three of these are in the same plane, and as a consequence, it may have similar binding ability to *Tri*-RNP regardless of the underlying RNA shape.

Constructing siRNA-Conjugated RNP Nanostructures To Control Gene Expression. In addition to protein modules, incorporation of RNA modules into the RNA scaffold[29,41−45] should expand the functionality of our RNP nanostructures. Thus, we investigated whether a functional small RNA module (*e.g.*, siRNA) could be incorporated into the same triangular RNP scaffold for gene expression control (Figure 5a). We designed LS-26 and *Tri*-26 conjugated with three siRNA strands targeting a GFP reporter (referred to as LS-26-siGFP and *Tri*-26-siGFP, respectively). The RNA nanostructure was composed of five types of RNA strands (S-26, L-26-1, L-26-2, L-26-3, and anti-GFP (AS)) to form three identical siRNA arms (Supporting Information Figure S14). The siGFP modules were designed to extend perpendicularly from each center of the three sides. We analyzed LS-26-siGFP and *Tri*-26-siGFP structures *in vitro* using AFM and clearly observed the nanostructures with three siGFP modules (Figure 5b). Without L7Ae, we observed heterogeneous RNA structures (*e.g.*, circular and triangular-like RNAs) with the three siRNA strands attached on the scaffold (Figure 5b, bottom). In contrast, with L7Ae, we observed a conformational change. We clearly observed the three L7Ae molecules on the three vertices and three siRNA strands protruding perpendicularly from each side, which confirmed the construction of *Tri*-26-siGFP *in vitro* (Figure 5b, top).

We next investigated whether the *Tri*-26-siGFP was recognized as a substrate for the dsRNA-cleaving enzyme Dicer. An *in vitro* Dicer cleavage assay showed that Dicer efficiently cleaved *Tri*-26-siGFP similarly to a control short hairpin RNA designed to knockdown GFP (sh-GFP)[46] (Figure 5c). These findings indicate that the three L7Ae-K-turn indications on *Tri*-26-siGFP scaffold do not inhibit Dicer activity through steric hindrance.

Finally, we tested whether the designed *Tri*-26-siGFP could produce functional siRNAs and knockdown the GFP target reporter within cells. *Tri*-26-siGFP, positive control sh-GFP, or LS-26-siGFP were transfected into HeLa cells with stable GFP expression (HeLa-GFP cells). We analyzed the GFP knockdown efficiencies in HeLa-GFP cells using flow cytometry and fluorescent microscopy; *Tri*-26-siGFP effectively repressed GFP expression depending on the siRNA module attached to the scaffold in a manner similar to the control sh-GFP or LS-26-siGFP (Figure 5d,e and Supporting Information Figure S15), indicating that *Tri*-26-siGFP scaffold with both protein and RNA modules can release functional siRNA and knockdown target gene within cells. Thus, we were able to construct and directly visualize functional RNPs with protein or RNA module in an RNA scaffold with enhanced stability and size control.

DISCUSSION

As an initial step toward generating a RNP-based molecular machine, we designed and constructed two functional RNP nanostructures: one includes AFB peptides that detect a specific breast cancer cell, and the other includes siRNA strands that knockdown the target gene expression in cells. Importantly, we directly visualized both the AFB and siRNA module-conjugated *Tri*-RNP at a single-molecule resolution. We clearly observed the three AFB molecules (58 amino acids)[39] or three siRNA strands (25 base pairs) attached on the triangular RNA scaffold (Figure 4c and Figure 5b). Through visualizing functional RNPs at high resolution, we provide the proof-of-concept for the RNP nanostructures. We can evaluate the nanostructure *in vitro* before it is used in practical cellular applications. We used this nanoscale triangular structure as a basic molecular scaffold to assemble functional modules for the following reasons: (1) An equilateral triangle is one of the most stable and simple geometrical structures. (2) Three functional protein modules (*e.g.*, a cell surface recognition peptide fused to L7Ae) can be attached to the apexes of the RNA triangle to minimize steric hindrance between the proteins. In addition, desirable three RNA modules (*e.g.*, siRNA modules) could also be attached to the three sides of the triangle, which potentially generates a multifunctional agent for biological applications. (3) The RNP interaction could improve RNA nanostructure stability under physiological conditions (Figure 3 and Supporting Information Figure S9). (4) The modules' orientation, distance, and functionality could be optimized by changing the underlying triangular scaffold size. In fact, *Tri*-26-AFB interacted with the target SKBR3 cells most effectively compared with the other constructs, such as *Tri*-70-AFB or *Tri*-92-AFB (Figure 4d). This result may have been due to several possible factors, including different RNP triangular structural stabilities on the cell surface as observed using AFM (Figure 2a, comparison between *Tri*-92 and *Tri*-26) or an effect of RNA scaffold size, which may optimize the interaction between *Tri*-AFB and the target SKBR3 cell surface receptors. Although a detailed mechanism on the effect of *Tri*-RNP size is currently under investigation, this result suggests that synthetic RNA scaffolds with an optimal size could

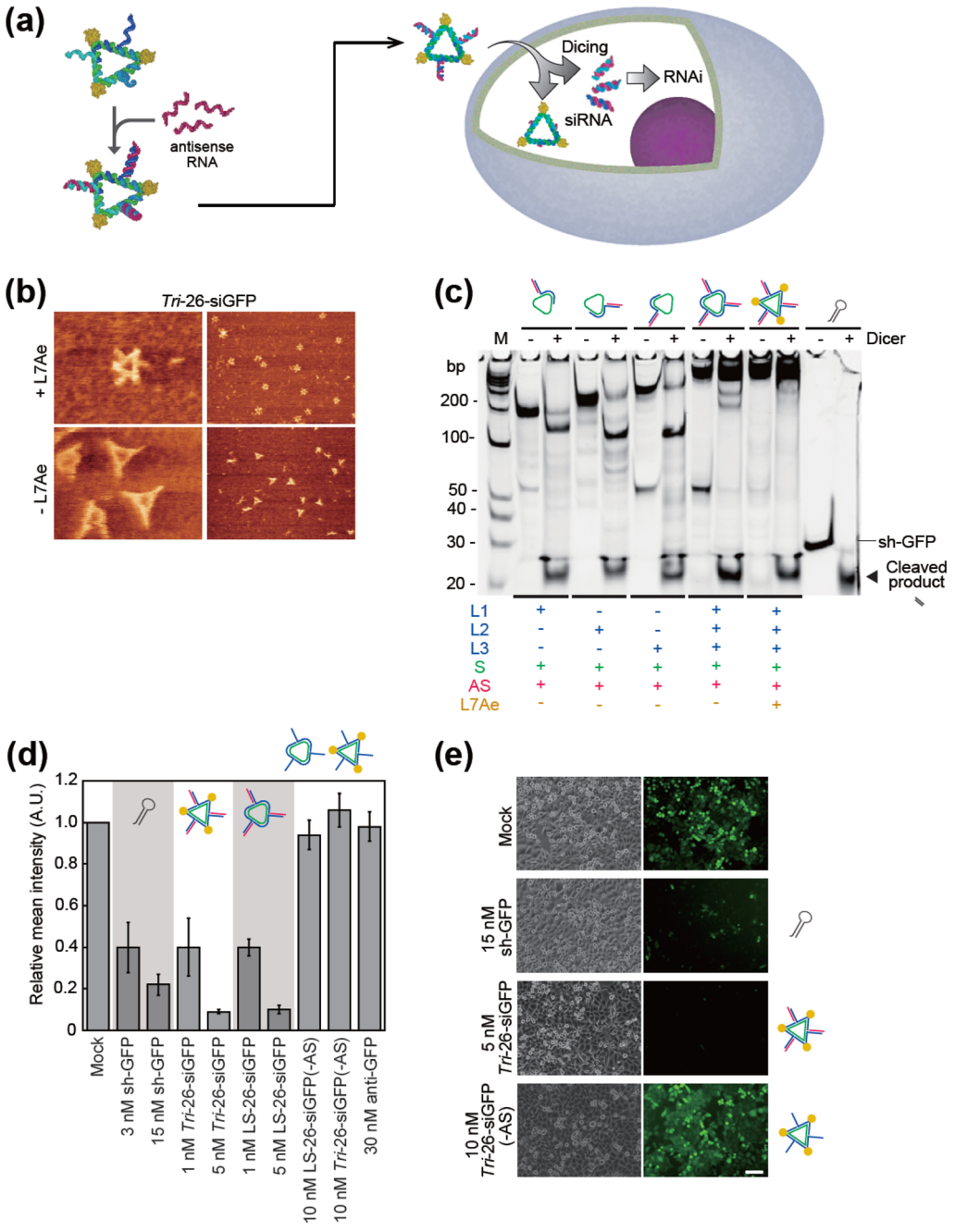

Figure 5. Construction and visualization of RNP nanostructures with RNAi activity. (a) Construction of the siRNA-conjugated RNP nanostructure (*Tri*-26-siGFP). The LS-26-siGFP or *Tri*-26-siGFP was composed of five types of RNA (S-26, L-26-1, L-26-2, L-26-3, and anti-GFP RNAs; see Supporting Information Figure S14). The size and sequence were based on *Tri*-26. The designed RNP induces RNAi in cells. (b) AFM images of the *Tri*-26-siGFP (top) and LS-26-siGFP (bottom). The AFM images were collected using 50 nM LS-26-siGFP with 600 nM L7Ae (top) or 50 nM LS-26-siGFP only (bottom). AFM images (100 nm × 75 nm, left, and 500 nm × 375 nm, right). (c) *In vitro* Dicer cleavage assay. The Dicer enzyme recognized and processed the siRNAs on LS-26-siGFP or *Tri*-26-siGFP. L-1, L-26-1; L-2, L-26-2; L-3, L-26-3 strands; S, short strand; and AS, anti-GFP. Native PAGE was used to identify the diced products. (+) Sample incubated with Dicer for 16 h at 37 °C; (−) sample incubated at 37 °C for 16 h in dicing buffer without Dicer. sh-GFP was used as a positive control shRNA for Dicer processing. M indicates double-stranded RNA marker. (d) *Tri*-26-siGFP gene knockdown activities inside cells. HeLa-GFPs were transfected with *Tri*-26-siGFP or LS-26-siGFP. The level of GFP knockdown was measured through the GFP expression levels using flow cytometry. sh-GFP was used as positive control shRNA for GFP knockdown. Bars and error bars represent the mean ± sd, respectively, of two triplicate experiments (n = 6). (e) Fluorescence microscopic images of the cells analyzed in (d). The scale bar indicates 100 μm.

improve the attached modules' function by controlling their number, distance, or configuration.

We generated two functional RNPs that either detect target cells selectively or control gene expression in cells. Although *Tri*-26-siGFP showed similar gene knockdown activity compared with LS-26-siGFP, increased RNA stability *via* the tight RNP interaction (Figure 3) and combined functions of both the AFB

peptide and siRNA modules could be useful for future *in vivo* RNA delivery into target cells. Multifunctional RNPs that can sequentially detect, invade, and control gene expression could be designed and constructed by inserting other modules (*e.g.*, cell membrane-penetrating or endosome-escaping modules) into the RNA scaffold.[46−48]

In previous studies, various RNA nanoparticles were designed and constructed.[28,29,43,49−52] However, these RNA-only nanostructures did not contain protein modules. In contrast, we constructed and precisely observed protein-controllable RNA nanostructures in which single RNA-binding protein (L7Ae) specifically binds to the target RNA motif (K-turn) on the designed RNA scaffold and dynamically regulates the formation of nanostructures. Moreover, we successfully and directly visualized formation of RNA−protein nanostructures in solution by time-lapse AFM imaging.

CONCLUSION

We constructed and directly visualized functional RNP and applied them to cellular applications, such as target breast cancer cell recognition at its cell surface and gene expression control inside a cell. The RNA scaffold size and conformation were controlled through RNA-strand and RNA-binding protein design, respectively. We believe that the functional RNP nanostructures constructed using this approach may be used to develop molecular machines that control living cell function in the extracellular and intracellular environments.

EXPERIMENTAL SECTION

Molecular Design of RNP Nanostructures with Different Sizes. We modified a previously reported molecular design protocol.[31] The three-dimensional atomic model for L7Ae-box C/D K-turn and affibody$_{ZHER2:342}$ was acquired from the PDB (ID: L7Ae, 1RLG; Affibody, 3MZW).[31,39] This modified L7Ae-K-turn structural model was used to design triangular RNPs (*Tri*-15, *Tri*-26, *Tri*-48, *Tri*-70, *Tri*-92, *Tri*-26$_{mut1}$, *Tri*-26$_{mut2}$, *Tri*-26$_{mut3}$, *Tri*-AFB, and *Tri*-siGFP) as follows. Three identical L7Ae-K-turn motifs were connected to form an equilateral triangle using three linear RNA double helices (the triangular RNA included Watson−Crick base pairs to support the triangular RNP nanostructures). An affibody$_{ZHER2:342}$ (AFB) molecule with a flexible linker $(SSSSG)_3$ at the N-terminus was fused to the L7Ae C-terminus (L7Ae-AFB). The L7Ae-AFB protein was used to design *Tri*-AFB. We constructed *Tri*-siGFP in a similar manner to a previous report.[45] The RNP molecules were designed using Discovery Studio software (Accelrys).

RNA Preparation. The DNA template, primers, and anti-GFP RNA used herein were purchased from Greiner (see Supporting Information Table S1). The DNA templates for *in vitro* transcription were generated using PCR with KOD-Plus-Neo DNA polymerase (Toyobo) (see Supplementary Methods). The RNA molecules were transcribed *in vitro* using a MEGAshortscript T7 kit (Ambion). Denaturing polyacrylamide gel electrophoresis (PAGE) was performed to purify the transcripts. After recovering the RNA, the RNA concentration was measured using a NanoDrop spectrophotometer (Thermo Scientific). For optical imaging and flow cytometry, the RNA strands were labeled using the ULYSIS Alexa Fluor 647 nucleic acid labeling kit (Invitrogen) in accordance with the manufacturer's protocol.

Cell Culture. The human breast cancer cell lines SKBR3, MCF-7, and MDA-MB-231 were acquired from the American Type Culture Collection (ATCC). The cells were cultured using McCoy's 5A (SKBR3) and RPMI culture media (MCF-7 and MDA-MB-231). Both media were supplemented with 10% fetal bovine serum (FBS) and either 1% penicillium-streptomycin (SKBR3), 1% antibiotics-antimycotic solution (MCF-7), or 0.1% gentamicin (MDA-MB-231).

Recombinant Protein Preparation. We modified the previously reported L7Ae expression and purification protocol.[31] L7Ae-AFB was purified *via* its hexahistidine tag. Briefly, the pET-28b(+) vector (Novagen) was used to clone and express the L7Ae-AFB protein. *Escherichia coli* Rosetta(DE3)/pLysS pRARE2 cells were transformed with the pET-28b(+) L7Ae-AFB plasmid. Protein expression was induced by adding 1 mM isopropyl β-D-1-thiogalactopyranoside (IPTG), and the cells were grown for 4 h at 37 °C. The cells were harvested through centrifugation at 4000*g* and 4 °C for 10 min and then resuspended in sonication buffer (20 mM phosphate buffer, pH 7.0, 500 mM NaCl, 2 mM $MgCl_2$, and 2.5 mM imidazole) with 2.4 U/mL benzonase (Novagen) at 4 °C. The supernatant was purified through nickel-chelate affinity chromatography using a HisTrap column (GE Healthcare) with a linear gradient elution from buffer A (20 mM phosphate buffer, pH 7.0, 500 mM NaCl, and 20 mM imidazole) to buffer B (20 mM phosphate buffer, pH 7.0, 500 mM NaCl, and 500 mM imidazole) by AKTA system (GE Healthcare). To remove nucleotides, the recombinant L7Ae-AFB was washed out following elution in a buffer (20 mM phosphate buffer, pH 7.0, 500 mM NaCl, and 2.5 mM imidazole) with 0.1 N NaOH and washed in washing buffer (20 mM phosphate buffer, pH 7.0, 500 mM NaCl, and 20 mM imidazole). The eluted protein was dialyzed against dialysis buffer (20 mM HEPES-KOH, pH 7.5, 150 mM KCl, 1.5 mM $MgCl_2$, and 40% glycerol) and stored at −30 °C for future use.

Electrophoretic Mobility Shift Assay (EMSA). Mixtures with 0.5 μL of each L- and S-strand RNA (final concentration, 50 nM), 2 μL of 5× RNP binding buffer (final concentration, 20 mM HEPES-KOH (pH 7.5), 150 mM KCl, and 1.5 mM $MgCl_2$), and 6 μL of Milli-Q purified water were heated to 80 °C for 3 min and then cooled at room temperature for 10 min to fold the LS-RNA. After adding 1 μL of the 10× protein solution, the mixtures were incubated at room temperature for approximately 30 min to facilitate binding between the RNA and protein. The mixtures were analyzed using a native polyacrylamide gel with 0.5× Tris/borate/EDTA buffer at room temperature. After electrophoresis, the gels were stained with SYBR Green I and II (Lonza) and observed using Typhoon FLA-7000 laser scanner (GE Healthcare).

High-Speed Atomic Force Microscopy (HS-AFM). The LS-RNA and RNP nanostructures were observed in solution. The LS-RNA or RNP samples were prepared as described for the EMSA. The AFM images were collected using high-speed AFM (Nano Live Vision, Research Institute of Biomolecules Metrology Co.) and small cantilevers with the dimensions ($L \times W \times H$) of $10 \times 2 \times 0.1$ μm^3 (BL-AC10EGS, Olympus Corporation). The cantilevers had a spring constant of 0.1−0.2 N/m with a resonant frequency of 400−1000 kHz in water. A sharp probe was deposited on each cantilever using electron beam deposition using a Nanotools instrument (Munich). The 320 × 240 pixel images were collected at the scan rate of 0.2−1.0 frames per second (fps). A fresh mica surface was coated with 0.1% APTES ((3-aminopropyl)-triethoxysilane). The samples (50 nM LS-RNA with or without 300 nM protein) were prepared in RNP binding buffer and diluted 10-fold with AFM observation buffer (20 mM Tris-HCl, pH 7.6, and 10 mM $MgCl_2$) and then applied to the mica for 5 min at room temperature and washed with the buffer solution. The image sequences were analyzed using ImageJ (http://rsb.info.nih.gov/ij/) and WSxM (http://www.nanotech.es/products/wsxm/index.php) software.

HS-AFM Time-Lapse Imaging of RNP Interactions and Conformations. The time-lapse images were acquired using HS-AFM. The scanning rate was 0.2 fps. A fresh mica surface was coated with 0.1% APTES. We applied LS-26 RNA diluted 10-fold with AFM

observation buffer (final concentration: 5 nM) to the mica for 5 min at room temperature and then washed with the buffer solution. After the mica surface was coated with LS-26 RNA, 100 nM L7Ae was directly added to begin scanning. The videos and images were rendered to show only the molecules of interest (Supporting Information movies S1 and S2). The timing of L7Ae binding to the RNA depended on the image collected, although the three L7Ae-three-K-turn interactions formed triangular structures under the experimental conditions (Figure 2c and Supporting Information Figure S8). To analyze the effect of the L7Ae-K-turn interaction shown in Supporting Information Figure S8b, representative *Tri*-48 structures were initially used to investigate the effect of L7Ae-AFB dissociation from *Tri*-48 during visualization. The image sequences were analyzed using ImageJ and WSxM software.

Analysis of LS-RNA/*Tri*-RNP Stabilities in the Presence of Serum. We used 50 nM LS-26 or 50 nM LS-26 and 300 nM L7Ae to produce *Tri*-26, which were treated with fetal bovine serum (FBS) (Figure 3) or human serum (Supporting Information Figure S9b). We first incubated *Tri*-26 or LS-26 in 20% serum without adding phenol. After incubating for a certain period of time (0, 30, 60, or 120 min), we added phenol and 10 mM EDTA (pH 8.0) to inactivate RNases in serum. The inactivation of RNases before electrophoresis protects RNA from further degradation during electrophoresis. After electrophoresis, the gels were stained with SYBR Green I and II and visualized using a Typhoon FLA-7000 laser scanner. *Tri*-26_{mut3} was used as a negative control for *Tri*-26 stability.

Flow Cytometry Analysis for the Cell Detection Assays. SKBR3, MCF-7, and MDA-MB-231 cells were seeded on a 24-well plate and incubated for prior to the cell recognition assay. After incubation, FBS was removed from the cell culture and the cells were rinsed with Opti-MEM medium three times. The cells were then treated with 10 nM *Tri*-26-AFB or 10 nM LS-26 for 1 h at 37 °C under 5% CO_2. We used 10 nM LS-26 and 30 nM L7Ae-AFB to produce 10 nM *Tri*-26-AFB. Subsequently, the cells were rinsed three times with Opti-MEM. We used flow cytometry with the BD Accuri (BD Biosciences) to measure the *Tri*-26-AFB cell-binding capacity. For the analysis using BD Accuri, a 675/25 nm filter was used to detect Alexa-647-labeled LS-RNA. After removing the dead cell population, we normalized the interacting cells' relative mean intensity (au) to the 10 nM LS-RNA-treated values.

Confocal Microscopy. SKBR3, MCF-7, and MDA-MB-231 cells were treated with 10 nM LS-26 or *Tri*-26-AFB for 1 h at 37 °C under 5% CO_2. After incubation, the cells were rinsed three times with Opti-MEM medium and stained with Hoechst 33342 (Invitrogen) for 15 min at 37 °C under 5% CO_2. After incubation, the cells were rinsed three times with Opti-MEM medium; fresh Opti-MEM medium was then added. The samples were visualized using a confocal laser scanning microscope A1R (Nikon). For the analysis using A1R, a 450/50 nm filter and a 700/75 nm filter were used to detect Hoechst 33342 and Alexa-647-labeled LS-RNA, respectively.

Molecular Design of *Tri*-26-siGFP and *In Vitro* Treatment with Human Dicer. To design *Tri*-26-siGFP, we prepared the LS-RNA region composed of five types of RNAs: S-26, L-26-1, L-26-2, L-26-3, and anti-GFP. The interaction among L-26-1, L-26-2, L-26-3, and anti-GFP forms three siRNA duplexes that knockdown GFP (Supporting Information Figure S14). The LS-26-siGFP and *Tri*-26-siGFP size and sequence are based on *Tri*-26. For *in vitro* Dicer cleavage assay, we mixed 500 nM LS-26-siGFP or 500 nM LS-26-siGFP and 3 μM L7Ae to produce 500 nM *Tri*-26-siGFP with 1 μL of 10 mM ATP, 0.5 μL of 50 mM $MgCl_2$, 4 μL of Dicer reaction buffer, 1 μL of recombinant Dicer enzyme (Genlantis), and water (to 10 μL). The mixtures were incubated at 37 °C for 16 h, and the incubation was arrested by adding 2 μL of Dicer stop solution. Native PAGE gels were used to identify the dicing products. After electrophoresis, the gels were stained with SYBR Green I and II and observed using a Typhoon FLA-7000 laser scanner.

RNAi Assays. HeLa cells that stably express *Hyg/GFP* (HeLa-GFP) were kindly provided by Dr T. Katoh and T. Suzuki (The University of Tokyo) and used to transfect LS-26-siGFP or *Tri*-26-siGFP. Hyg/EGFP gene expresses EGFP fused with a hygromycin resistance gene. The HeLa-GFP cells were cultured in DMEM-F12 medium with 10% FBS, 1% antibiotic–antimycotic solution, and 0.1% hygromycin B at 37 °C and 5% CO_2. A total of 5×10^4 cells were seeded in 24-well plates, and 70–90% confluent cells were transiently transfected with 0.25 or 1.25 pmol LS-26-siGFP (final concentration 1 or 5 nM), 0.25 or 1.25 pmol *Tri*-26-siGFP (final concentration 1 or 5 nM), 1.25 pmol LS-26-siGFP (-AS) (final concentration 5 nM), 1.25 pmol *Tri*-26-siGFP (-AS) (final concentration 5 nM), 0.75 or 3.75 pmol sh-GFP (final concentration 3 or 15 nM), and 7.5 pmol anti-GFP (final concentration 30 nM) for GFP using 0.52 μL of Stemfect reagent (Stemgent) following the manufacturer's instructions. Four hours after transfection, the culture medium was replaced with fresh medium. Twenty-four hours after transfection, the cells were washed with Opti-MEM medium and analyzed with fluorescence microscopy (BIOREVO BZ-9000, KEYENCE). After the fluorescence microscopic analysis, the cells were incubated in 200 μL of 0.25% Trypsin-EDTA (GIBCO) for 3 min at 37 °C and added to 200 μL of FACS buffer (PBS containing 5% FBS), and then the GFP expression levels were analyzed with flow cytometer BD Accuri. A 488 nm semiconductor laser and 533/30 nm filter was used for GFP expression detection. We constructed *Tri*-26-siGFP by mixing LS-26-siGFP and L7Ae at 1:3 molar ratio. For example, we used 1 nM LS-26-siGFP and 3 nM L7Ae to produce 1 nM *Tri*-26-siGFP. sh-GFP was used as positive GFP knockdown control.

Conflict of Interest: The authors declare the following competing financial interest(s): The authors declare the following competing financial interests: Kyoto University will file a patent application broadly relevant to this work. E. Osada and H. Saito are the investigators of record listed on the patent application.

Acknowledgment. The authors thank Y. Fujita, R. Furushima, K. Endo, S. Kashida, and T. Inoue (Kyoto University) for fruitful discussions; H. Kawabata and N. Nishimura (Kyoto University) for RNP nanostructure purification and cell culture. We also thank C. Parr (Kyoto University), Y. Shimizu (RIKEN), and M. Takinoue (Tokyo Institute Technology) for critically reading the manuscript. This work was supported by the New Energy and Industrial Technology Development Organization (09A02021a) (H.S.), Grant-in-Aid for Young Scientists (A) (No. 23681042) (H.S.), Grant-in-Aid for Young Scientists (B) (No. 25870383) (E.O.), and a Grant-in-Aid for Scientific Research on Innovative Areas "Molecular Robotics" (No. 24104002) from The Ministry of Education, Culture, Sports, Science, and Technology, Japan.

Supporting Information Available: Detailed experimental procedure, sequence of RNA nanostructure and DNA used in this study, additional EMSA, HS-AFM images, HS-AFM movies and all analysis data. This material is available free of charge *via* the Internet at http://pubs.acs.org.

REFERENCES AND NOTES

1. Bleichert, F.; Baserga, S. J. Ribonucleoprotein Multimers and Their Functions. *Crit. Rev. Biochem. Mol. Biol.* **2010**, *45*, 331–350.
2. Staley, J. P.; Woolford, J. L., Jr. Assembly of Ribosomes and Spliceosomes: Complex Ribonucleoprotein Machines. *Curr. Opin. Cell Biol.* **2009**, *21*, 109–118.
3. Ramaswami, M.; Taylor, J. P.; Parker, R. Altered Ribostasis: RNA–Protein Granules in Degenerative Disorders. *Cell* **2013**, *154*, 727–736.
4. Leung, E. K.; Suslov, N.; Tuttle, N.; Sengupta, R.; Piccirilli, J. A. The Mechanism of Peptidyl Transfer Catalysis by the Ribosome. *Annu. Rev. Biochem.* **2011**, *80*, 527–555.
5. Turner, B.; Melcher, S. E.; Wilson, T. J.; Norman, D. G.; Lilley, D. M. Induced Fit of RNA on Binding the L7Ae Protein to the Kink-Turn Motif. *RNA* **2005**, *11*, 1192–1200.
6. Law, M. J.; Rice, A. J.; Lin, P.; Laird-Offringa, I. A. The Role of RNA Structure in the Interaction of U1A Protein with U1 Hairpin II RNA. *RNA* **2006**, *12*, 1168–1178.
7. Wang, J.; Fessl, T.; Schroeder, K. T.; Ouellet, J.; Liu, Y.; Freeman, A. D.; Lilley, D. M. Single-Molecule Observation of the Induction of K-Turn RNA Structure on Binding L7Ae Protein. *Biophys. J.* **2012**, *103*, 2541–2548.
8. Pinheiro, A. V.; Han, D.; Shih, W. M.; Yan, H. Challenges and Opportunities for Structural DNA Nanotechnology. *Nat. Nanotechnol.* **2011**, *6*, 763–772.

9. Simmel, F. C. DNA-Based Assembly Lines and Nanofactories. *Curr. Opin. Biotechnol.* **2012**, *23*, 516–521.
10. Liu, M.; Fu, J.; Hejesen, C.; Yang, Y.; Woodbury, N. W.; Gothelf, K.; Liu, Y.; Yan, H. A DNA Tweezer-Actuated Enzyme Nanoreactor. *Nat. Commun.* **2013**, *4*, 2127–2131.
11. Zhang, C.; Tian, C.; Guo, F.; Liu, Z.; Jiang, W.; Mao, C. DNA-Directed Three-Dimensional Protein Organization. *Angew. Chem., Int. Ed.* **2012**, *51*, 3382–3385.
12. Douglas, S. M.; Bachelet, I.; Church, G. M. A Logic-Gated Nanorobot for Targeted Transport of Molecular Payloads. *Science* **2012**, *335*, 831–834.
13. Schuller, V. J.; Heidegger, S.; Sandholzer, N.; Nickels, P. C.; Suhartha, N. A.; Endres, S.; Bourquin, C.; Liedl, T. Cellular Immunostimulation by CpG-Sequence-Coated DNA Origami Structures. *ACS Nano* **2011**, *5*, 9696–9702.
14. Rudchenko, M.; Taylor, S.; Pallavi, P.; Dechkovskaia, A.; Khan, S.; Butler, V. P., Jr.; Rudchenko, S.; Stojanovic, M. N. Autonomous Molecular Cascades for Evaluation of Cell Surfaces. *Nat. Nanotechnol.* **2013**, *8*, 580–586.
15. Lee, H.; Lytton-Jean, A. K.; Chen, Y.; Love, K. T.; Park, A. I.; Karagiannis, E. D.; Sehgal, A.; Querbes, W.; Zurenko, C. S.; Jayaraman, M.; *et al.* Molecularly Self-Assembled Nucleic Acid Nanoparticles for Targeted *In Vivo* siRNA Delivery. *Nat. Nanotechnol.* **2012**, *7*, 389–393.
16. Murata, S.; Konagaya, A.; Kobayashi, S.; Saito, H.; Hagiya, M. Molecular Robotics: A New Paradigm for Artifacts. *New Gener. Comput.* **2013**, *31*, 27–45.
17. Guo, P. The Emerging Field of RNA Nanotechnology. *Nat. Nanotechnol.* **2010**, *5*, 833–842.
18. Grabow, W.; Jaeger, L. RNA Modularity for Synthetic Biology. *F1000Prime Rep.* **2013**, *5*, 46–55.
19. Shu, Y.; Pi, F.; Sharma, A.; Rajabi, M.; Haque, F.; Shu, D.; Leggas, M.; Evers, B. M.; Guo, P. Stable RNA Nanoparticles as Potential New Generation Drugs for Cancer Therapy. *Adv. Drug Delivery Rev.* **2014**, *66*, 74–89.
20. Guo, P. RNA Nanotechnology: Engineering, Assembly and Applications in Detection, Gene Delivery and Therapy. *J. Nanosci. Nanotechnol.* **2005**, *5*, 1964–1982.
21. Jossinet, F.; Ludwig, T. E.; Westhof, E. RNA Structure: Bioinformatic Analysis. *Curr. Opin. Microbiol.* **2007**, *10*, 279–285.
22. McNamara, J. O., II; Andrechek, E. R.; Wang, Y.; Viles, K. D.; Rempel, R. E.; Gilboa, E.; Sullenger, B. A.; Giangrande, P. H. Cell Type-Specific Delivery of siRNAs with Aptamer-siRNA Chimeras. *Nat. Biotechnol.* **2006**, *24*, 1005–1015.
23. Saito, H.; Kobayashi, T.; Hara, T.; Fujita, Y.; Hayashi, K.; Furushima, R.; Inoue, T. Synthetic Translational Regulation by an L7Ae-Kink-Turn RNP Switch. *Nat. Chem. Biol.* **2010**, *6*, 71–78.
24. Kashida, S.; Inoue, T.; Saito, H. Three-Dimensionally Designed Protein-Responsive RNA Devices for Cell Signaling Regulation. *Nucleic Acids Res.* **2012**, *40*, 9369–9378.
25. Culler, S. J.; Hoff, K. G.; Smolke, C. D. Reprogramming Cellular Behavior with RNA Controllers Responsive to Endogenous Proteins. *Science* **2010**, *330*, 1251–1255.
26. Cruz, J. A.; Westhof, E. Sequence-Based Identification of 3D Structural Modules in RNA with RMDetect. *Nat. Methods* **2011**, *8*, 513–521.
27. Delebecque, C. J.; Lindner, A. B.; Silver, P. A.; Aldaye, F. A. Organization of Intracellular Reactions with Rationally Designed RNA Assemblies. *Science* **2011**, *333*, 470–474.
28. Afonin, K. A.; Viard, M.; Martins, A. N.; Lockett, S. J.; Maciag, A. E.; Freed, E. O.; Heldman, E.; Jaeger, L.; Blumenthal, R.; Shapiro, B. A. Activation of Different Split Functionalities on Re-association of RNA–DNA Hybrids. *Nat. Nanotechnol.* **2013**, *8*, 296–304.
29. Afonin, K. A.; Kireeva, M.; Grabow, W. W.; Kashlev, M.; Jaeger, L.; Shapiro, B. A. Co-transcriptional Assembly of Chemically Modified RNA Nanoparticles Functionalized with siRNAs. *Nano Lett.* **2012**, *12*, 5192–5195.
30. Shu, Y.; Haque, F.; Shu, D.; Li, W.; Zhu, Z.; Kotb, M.; Lyubchenko, Y.; Guo, P. Fabrication of 14 Different RNA Nanoparticles for Specific Tumor Targeting without Accumulation in Normal Organs. *RNA* **2013**, *19*, 767–777.
31. Ohno, H.; Kobayashi, T.; Kabata, R.; Endo, K.; Iwasa, T.; Yoshimura, S. H.; Takeyasu, K.; Inoue, T.; Saito, H. Synthetic RNA–Protein Complex Shaped Like an Equilateral Triangle. *Nat. Nanotechnol.* **2011**, *6*, 116–120.
32. Moore, T.; Zhang, Y.; Fenley, M. O.; Li, H. Molecular Basis of Box C/D RNA–Protein Interactions; Cocrystal Structure of Archaeal L7Ae and a Box C/D RNA. *Structure* **2004**, *12*, 807–818.
33. Rozhdestvensky, T. S.; Tang, T. H.; Tchirkova, I. V.; Brosius, J.; Bachellerie, J. P.; Huttenhofer, A. Binding of L7Ae Protein to the K-Turn of Archaeal snoRNAs: A Shared RNA Binding Motif for C/D and H/ACA Box snoRNAs in Archaea. *Nucleic Acids Res.* **2003**, *31*, 869–877.
34. Klein, D. J.; Schmeing, T. M.; Moore, P. B.; Steitz, T. A. The Kink-Turn: A New RNA Secondary Structure Motif. *EMBO J.* **2001**, *20*, 4214–4221.
35. Rajendran, A.; Endo, M.; Sugiyama, H. State-of-the-Art High-Speed Atomic Force Microscopy for Investigation of Single-Molecular Dynamics of Proteins. *Chem. Rev.* **2014**, *114*, 1493–1520.
36. Suzuki, Y.; Gilmore, J. L.; Yoshimura, S. H.; Henderson, R. M.; Lyubchenko, Y. L.; Takeyasu, K. Visual Analysis of Concerted Cleavage by Type IIF Restriction Enzyme SfiI in Subsecond Time Region. *Biophys. J.* **2011**, *101*, 2992–2998.
37. Kodera, N.; Yamamoto, D.; Ishikawa, R.; Ando, T. Video Imaging of Walking Myosin V by High-Speed Atomic Force Microscopy. *Nature* **2010**, *468*, 72–76.
38. Shinozaki, Y.; Sumitomo, K.; Tsuda, M.; Koizumi, S.; Inoue, K.; Torimitsu, K. Direct Observation of ATP-Induced Conformational Changes in Single P2X(4) Receptors. *PLoS Biol.* **2009**, *7*, e1000103.
39. Orlova, A.; Magnusson, M.; Eriksson, T. L.; Nilsson, M.; Larsson, B.; Hoiden-Guthenberg, I.; Widstrom, C.; Carlsson, J.; Tolmachev, V.; Stahl, S.; *et al.* Tumor Imaging Using a Picomolar Affinity HER2 Binding Affibody Molecule. *Cancer Res.* **2006**, *66*, 4339–4348.
40. Eigenbrot, C.; Ultsch, M.; Dubnovitsky, A.; Abrahmsen, L.; Hard, T. Structural Basis for High-Affinity HER2 Receptor Binding by an Engineered Protein. *Proc. Natl. Acad. Sci. U.S.A.* **2010**, *107*, 15039–15044.
41. Afonin, K. A.; Desai, R.; Viard, M.; Kireeva, M. L.; Bindewald, E.; Case, C. L.; Maciag, A. E.; Kasprzak, W. K.; Kim, T.; Sappe, A.; *et al.* Co-Transcriptional Production of RNA–DNA Hybrids for Simultaneous Release of Multiple Split Functionalities. *Nucleic Acids Res.* **2014**, *42*, 2085–2097.
42. Grabow, W. W.; Zakrevsky, P.; Afonin, K. A.; Chworos, A.; Shapiro, B. A.; Jaeger, L. Self-Assembling RNA Nanorings Based on RNAI/II Inverse Kissing Complexes. *Nano Lett.* **2011**, *11*, 878–887.
43. Shu, Y.; Shu, D.; Haque, F.; Guo, P. Fabrication of pRNA Nanoparticles To Deliver Therapeutic RNAs and Bioactive Compounds into Tumor Cells. *Nat. Protoc.* **2013**, *8*, 1635–1659.
44. Guo, P.; Haque, F.; Hallahan, B.; Reif, R.; Li, H. Uniqueness, Advantages, Challenges, Solutions, and Perspectives in Therapeutics Applying RNA Nanotechnology. *Nucleic Acid Ther.* **2012**, *22*, 226–245.
45. Afonin, K. A.; Grabow, W. W.; Walker, F. M.; Bindewald, E.; Dobrovolskaia, M. A.; Shapiro, B. A.; Jaeger, L. Design and Self-Assembly of siRNA-Functionalized RNA Nanoparticles for Use in Automated Nanomedicine. *Nat. Protoc.* **2011**, *6*, 2022–2034.
46. Saito, H.; Fujita, Y.; Kashida, S.; Hayashi, K.; Inoue, T. Synthetic Human Cell Fate Regulation by Protein-Driven RNA Switches. *Nat. Commun.* **2011**, *2*, 160–167.
47. Endoh, T.; Sisido, M.; Ohtsuki, T. Cellular siRNA Delivery Mediated by a Cell-Permeant RNA-Binding Protein and Photoinduced RNA Interference. *Bioconjugate Chem.* **2008**, *19*, 1017–1024.
48. Nakase, I.; Hirose, H.; Tanaka, G.; Tadokoro, A.; Kobayashi, S.; Takeuchi, T.; Futaki, S. Cell-Surface Accumulation of Flock House Virus-Derived Peptide Leads to Efficient Internalization *via* Macropinocytosis. *Mol. Ther.* **2009**, *17*, 1868–1876.

49. Chworos, A.; Severcan, I.; Koyfman, A. Y.; Weinkam, P.; Oroudjev, E.; Hansma, H. G.; Jaeger, L. Building Programmable Jigsaw Puzzles with RNA. *Science* **2004**, *306*, 2068–2072.
50. Zhang, H.; Endrizzi, J. A.; Shu, Y.; Haque, F.; Sauter, C.; Shlyakhtenko, L. S.; Lyubchenko, Y.; Guo, P.; Chi, Y. I. Crystal Structure of 3WJ Core Revealing Divalent Ion-Promoted Thermostability and Assembly of the Phi29 Hexameric Motor pRNA. *RNA* **2013**, *19*, 1226–1237.
51. Afonin, K. A.; Bindewald, E.; Yaghoubian, A. J.; Voss, N.; Jacovetty, E.; Shapiro, B. A.; Jaeger, L. *In Vitro* Assembly of Cubic RNA-Based Scaffolds Designed *in Silico*. *Nat. Nanotechnol.* **2010**, *5*, 676–682.
52. Severcan, I.; Geary, C.; Chworos, A.; Voss, N.; Jacovetty, E.; Jaeger, L. A Polyhedron Made of tRNAs. *Nat. Chem.* **2010**, *2*, 772–779.